



ISTITUTO NAZIONALE DI RICERCA METROLOGICA Repository Istituzionale

Characterization of nanodiamond samples for intracellular temperature sensing

Original

Characterization of nanodiamond samples for intracellular temperature sensing / Stella, Claudia; Moreva, Ekaterina; Bernardi, Ettore; Losero, Elena; Traina, Paolo; Degiovanni, Ivo Pietro; Tomagra, Giulia; Carabelli, Valentina; Cígler, Petr; Genovese, Marco. - In: MEASUREMENT. SENSORS. - ISSN 2665-9174. - 38:(2025). [10.1016/j.measen.2024.101650]

Availability:

This version is available at: 11696/89239 since: 2026-03-10T10:34:59Z

Publisher:

Elsevier Ltd

Published

DOI:10.1016/j.measen.2024.101650

Terms of use:

This article is made available under terms and conditions as specified in the corresponding bibliographic description in the repository

Publisher copyright

(Article begins on next page)



Characterization of nanodiamond samples for intracellular temperature sensing

ARTICLE INFO

Keywords:

NV centers
ODMR
Quantum sensing
Intracellular temperature sensing
Biology

ABSTRACT

Nitrogen-Vacancy (NV) center in nanodiamonds offers unique advantages for thermometry applied in biological samples. Small size and biocompatibility make nanodiamonds promising as nanoscale thermometers. The energy level structure of NV centers enables optical initialization and readout of the spin state, particularly in their triplet ground state, where the energy gap (D_{gs}) between $|m_s = 0\rangle$ and $|m_s = \pm 1\rangle$ is sensitive to environmental conditions. Variations in temperature, magnetic, or electric fields induce changes in the energy structure of the system, allowing for precise reconstruction of applied field values and facilitating the use of NV centers as sensors. The purpose of this work is to characterize the response of a set of nanodiamonds to a change in temperature: knowing the value of the coefficient that links the change in temperature to a change in D_{gs} makes possible to use nanodiamonds inside cells as thermometers. Moreover, some techniques that can reduce the uncertainty related to the estimation of this coupling constant are investigated.

1. Introduction

In the last 20 years specific properties of quantum systems become a tool for improving sensing and imaging [1,2] overpassing the limits of classical measurements [3]. Among these new methods colour centers in diamond (substantially realizing an “artificial atom”) were identified as very promising system due to their specific properties. Diamond is a chemically inert and biologically compatible material [4,5] that can occur in form of nanodiamonds (NDs), making it suitable for intracellular measurements. Another promising possibility is related to the functionalization of these nanodiamonds, in this way it will be possible to investigate specific areas inside cells such as mitochondria or ion channels. The use of diamond as a sensor is enabled by the presence of impurities within the crystalline matrix [6–8] and its use as a sensor in biological samples has been implemented in several studies [9–12], with recent findings demonstrating the capability to measure temperature changes correlated with actual physiological signals [13]. The possibility to exploit nanodiamonds as intracellular sensors leads to a better understanding of how temperature influences cellular mechanisms such as, for example, the speed of ion channel opening [14] or cells metabolism [15]. Conversely, it also allows us to observe how alterations in cellular activity, as may occur in neurodegenerative diseases, affect cellular temperature. To determine changes in temperature inside cells, it is necessary to understand how the resonance frequency depends on temperature [16] and to ensure complete decoupling from external fields.

1.1. NV-based ODMR technique

The most extensively studied and employed defect as a sensor is the complex formed by a nitrogen atom paired with a vacancy (NV-centers). This defect exhibits a triplet ground state (Fig. 1) wherein the levels

<https://doi.org/10.1016/j.measen.2024.101650>

Available online 10 January 2025

$|m_s = 0\rangle$ and $|m_s = \pm 1\rangle$ are energetically separated by approximately $D_{gs} \sim 2.87$ GHz (zero field splitting) [17,18].

Microwave fields can be applied to manipulate the ground state, populating the $|m_s = \pm 1\rangle$ state when the tuning in frequency occurs. Exposing the system to a green laser induces a continuous process of excitation and relaxation that initializes the system in $|m_s = 0\rangle$, this process is called optical initialization. Spin state readout is also possible; in fact, starting from the $|m_s = 0\rangle$ state the system relaxes through red light emission, but starting from the $|m_s = \pm 1\rangle$ state, relaxation of the system through visible emission is accompanied by a non-radiative relaxation pathway leading to a decrease in collected photoluminescence. The Optically Detected Magnetic Resonance (ODMR) [19, 20] is a technique that involves the simultaneous application of a variable microwave field, an excitation light source and collection of the emitted photoluminescence (PL). The result is an ODMR spectrum with a minimum corresponding to $f_{MW} = D_{gs}$. Since external fields induce a variation in the resonance frequency, by evaluating the displacement of D_{gs} it is possible to reconstruct the value of the applied fields [21].

1.2. Magnetic field sensing

In an unperturbed system, the states $|m_s = \pm 1\rangle$ are degenerate; however, this degeneracy can be removed by the presence of external fields or strain in crystalline matrix. The application of an external magnetic field leads to the removal of the degeneracy due to the Zeeman effect, resulting in a spectrum with two photoluminescence minima corresponding to the two different spin state transitions (Fig. 2). The frequency split between the two minima is proportional to the intensity of the applied field according to the following formula:

$$\Delta f_{m_s=\pm 1} = \frac{\mu_B g_e}{h} \cdot B_z \quad (1)$$

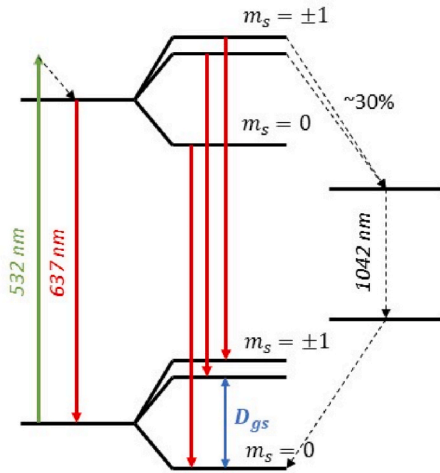


Fig. 1. Energy level diagram of NV-center.

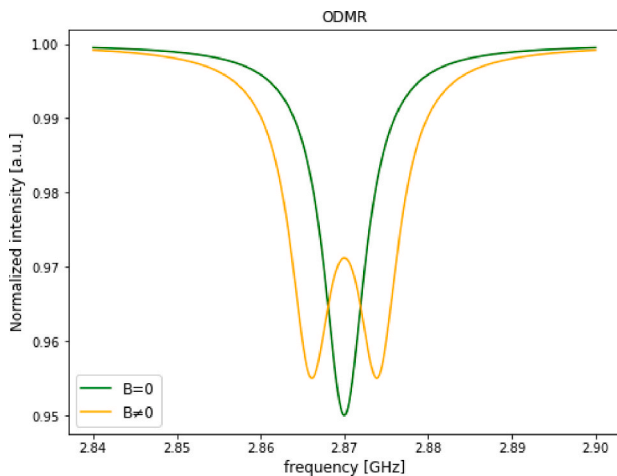


Fig. 2. Simulated ODMR spectrum with and without an applied magnetic field.

Where μ_B is the Bohr magneton, g_e is the Landé g-factor and B_z is the projection of the field on the NV axis.

Exploiting this phenomenon is possible to use diamond as quantum sensor for magnetic fields [22]. However, it's important to note that from a single NV only the component along z can be reconstructed, while with an ensemble of NVs a complete reconstruction of amplitude and orientation can be obtained [23].

1.3. Temperature sensing

Temperature variations alter the spin-spin interaction in the NV's orbital structures, leading to a change in the value of D_{gs} and a corresponding shift in the ODMR spectrum (Fig. 3) [24]. The relationship between D_{gs} and ΔT is given by:

$$\Delta D_{gs} = \frac{\partial D_{gs}}{\partial T} \cdot \Delta T = \gamma_T \cdot \Delta T \quad (2)$$

The parameter γ_T represents the coupling constant and it is estimated on average to be $\gamma_T = -75 \frac{\text{kHz}}{\text{K}}$ for bulk diamond [25,26]. For nanodiamonds the value of γ_T presents more variability, its value can take values from $65 \frac{\text{kHz}}{\text{K}}$ to $78 \frac{\text{kHz}}{\text{K}}$ [9,11,16,27–29], for this reason this parameter requires calibration. For the calibration it is important that spectrum variations are only due to temperature, thus requiring complete shielding from external field variations.

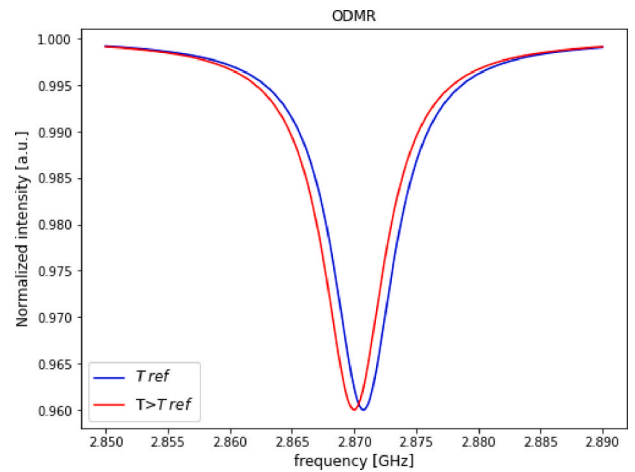


Fig. 3. Simulation of normalized ODMR spectrum at two different temperatures.

1.4. Differential ODMR for biological measurements

Although the use of nanodiamonds as intracellular temperature sensors proves to be very promising tool, attention must be paid to ensure that experimental conditions do not affect cellular activity [30, 31]. In particular, some parameters must be kept as low as possible such as the optical power of the laser, exposure time, and microwave intensity. A technique that reduces laser exposure time involves acquiring the ODMR spectrum just at the beginning of the experiment and using it to reconstruct a graph, referred as differential spectrum, where, for each frequency, the difference in signal intensity from its symmetric frequencies, scattered by a chosen f_{dev} , is plotted [32].

$$\tilde{F} = I(f + f_{dev}) - I(f - f_{dev}) \quad (3)$$

The obtained spectrum presents zeros corresponding to the minimum and a linear region around it, attributed to the peak's symmetry (See Fig. 4).

By exploiting the linearity of this spectrum around the minima, statistical data is collected only at a point within the linear region. In this way is possible to increase the statistics at the point of interest that allow

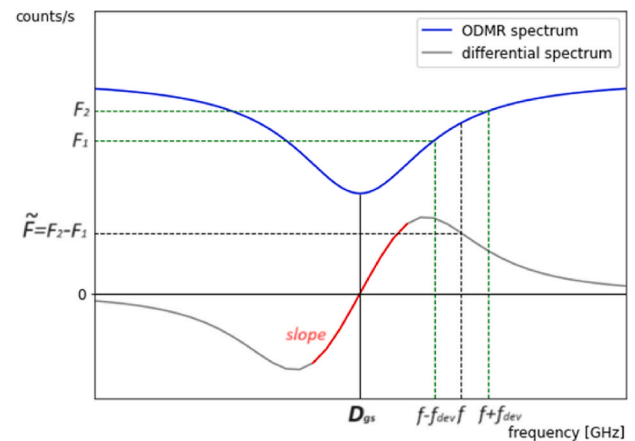


Fig. 4. Diagram illustrating the process of the differential measurement. The lower part of the figure shows the derived differential spectrum from the ODMR spectrum (upper part). For each microwave (MW) frequency value, the difference $\tilde{F} = F_1 - F_2$ in photoluminescence (PL) between two points (f_1, f_2) separated by $2f_{dev}$ is calculated. \tilde{F} is equals zero at the spectrum's extremes and at the resonant frequency D_{gs} . It is possible to appreciate that exists a region in which there is a linear dependency of $\Delta \tilde{F}$ on Δf near D_{gs} .

for the evaluation of ΔT according to this formula:

$$\left\{ \begin{array}{l} \tilde{F}_T - \tilde{F}_{T_{ref}} = \Delta \tilde{F} = slope \cdot \Delta D_{gs} \\ \Delta D_{gs} = \gamma_T \cdot \Delta T \end{array} \right. \rightarrow \Delta T = \frac{\Delta \tilde{F}}{slope \cdot \gamma_T} \quad (4)$$

2. Methods and procedures

This study aims to characterize a sample of nanodiamonds to estimate the coefficient γ_T for their utilization as intracellular temperature sensors. Calibration was performed both in the absence and presence of a Faraday cage for electromagnetic noise shielding. It was observed that the shielding significantly improves measurements stability.

2.1. Procedure

The calibration was performed by varying the temperature in a controlled way using an incubator, with the actual temperature measured by a thermocouple. Starting from a reference temperature of 37 °C, the temperature was incrementally lowered to a value of 25 °C, followed by a return to the reference temperature. For each temperature step, the $\Delta \tilde{F}$ signal, respect to T_{ref} , was evaluated. This approach allowed for the derivation of a curve, with the angular coefficient representing the coupling constant γ_T .

$$\Delta \tilde{F} = \gamma_T \cdot (slope \cdot \Delta T) \quad (5)$$

2.2. Setup

The experimental setup used in this study (Fig. 5) consisted of an Olympus IX73 inverted microscope, which included optical components for single-photon confocal imaging and microwave control for ODMR measurements.

A continuous wave (CW) 532nm laser (Coherent Prometheus 100NE) is used to excite the NV centers. A 60x air microscope objective

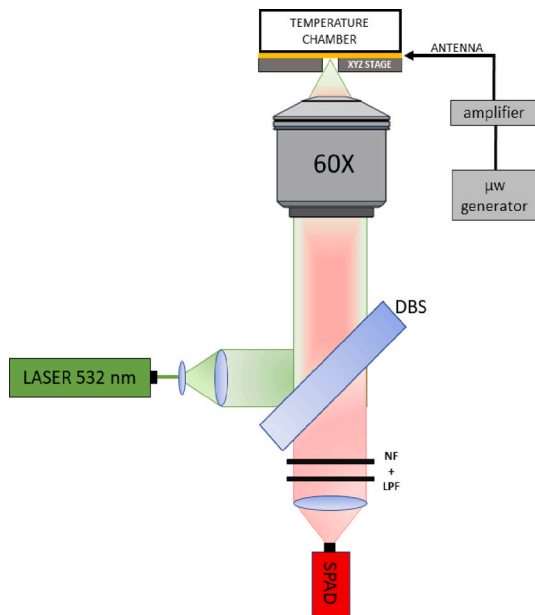


Fig. 5. Schematic of the experimental setup. This setup is composed by a green laser (532 nm) for the excitation of the system, a microwave generator for the application of variable MW field (μW generator), a temperature chamber placed on a software controlled xyz stage and a SPAD for the collection of the light. Along the optical path there is a 60x objective for the focalization and collection of the light, a 567 nm dichroic mirror (DBS) to cut the laser from the optical path to the detector, a neutral filter (NF) to avoid the saturation of the SPAD and a long pass filter (LPF) to cut the emission related to the phononic band of NV's spectrum.

(Olympus UPLANFL, NA = 0.67) is used for both excitation and photoluminescence (PL) collection.

The NV PL signal is filtered using a 567 nm dichroic mirror, a 650 nm long-pass filter, and a Notch filter centered at 532 nm to remove residual green laser scattering. Subsequently, the signal is collected by a single-photon avalanche diode (SPAD, SPCM-AQR 15, PerkinElmer), and then processed by a data acquisition board system (National Instruments, USB-6343 BNC).

A closed incubation chamber equipped with temperature control (Okolab Temperature Controller, with a temperature stability of 0.1 °C) is integrated into the setup to vary the temperature in controlled mode. A software controlled piezoelectric XYZ scanning stage allow to move the samples for the selection of a region with single isolated nanodiamond.

For ODMR measurements, a microwave source (Keysight N5172B) is used, with the output signal subsequently amplified (Mini-Circuits, ZHL 16W 43+). This amplified signal was then directed to a homemade planar broadband antenna, providing strong, homogeneous electromagnetic radiation [33]. The sample was placed on top of the antenna for measurements.

2.3. Nanodiamonds

The nanodiamonds (NDs) were provided by Microdiamant Switzerland (MSY 0–0.25), containing approximately 100–200 ppm of natural nitrogen impurities.

Initially, the NDs underwent oxidation by exposure to air oxygen at 510 °C for 5 hours. Subsequently, they were subjected to wet oxidation in a stirred mixture of HF:HNO₃ (2:1 v/v) at 160 °C for 2 days within a PTFE container. The acids were removed through consecutive centrifugation and washing steps, resulting in pure oxidized NDs, which were then lyophilized.

To isolate monodisperse NDs with a hydrodynamic diameter of 205 nm, a process involving differential centrifugation in water was employed. This process included gradual centrifugation and dilution steps, combination of separated pellets, and subsequent lyophilization.

In order to increase the NV density, 330 mg of monodisperse NDs were irradiated at 870 °C for 80 hours in an external target using a 15.7 MeV electron beam (2.5×10^{19} particles cm⁻²) extracted from the MT-25 microtron. Following irradiation, the NDs (315 mg) were annealed at 900 °C for 1 hour under an argon atmosphere and then oxidized in air for 5 hours at 510 °C.

Before utilization, the lyophilized NDs were redispersed in Milli-Q water via cup horn sonication to achieve a concentration of 1.0 mg mL⁻¹.

3. Results and discussion

3.1. Calibration without shielding

The first datasets were acquired without shielding from external fields variations. Following the procedure exposed in section 2.1. four data were collected. The result is shown in Fig. 6. From these calibration curves is evident that the contribution of external fields is not negligible for measurements lasting over time, in fact, the data results significantly scattered from the fitted curve.

The coupling constant obtained from each calibration curve as angular coefficient of the linear fitting and its associated uncertainty is reported in Table 1.

3.2. Calibration with shielding

The second datasets were obtained by shielding the system with a Faraday cage (see Table 2). The procedure is analogous to the previous measurement, and the results are shown in Fig. 7. In contrast to the previous dataset, in this case, it is possible to appreciate that all the data

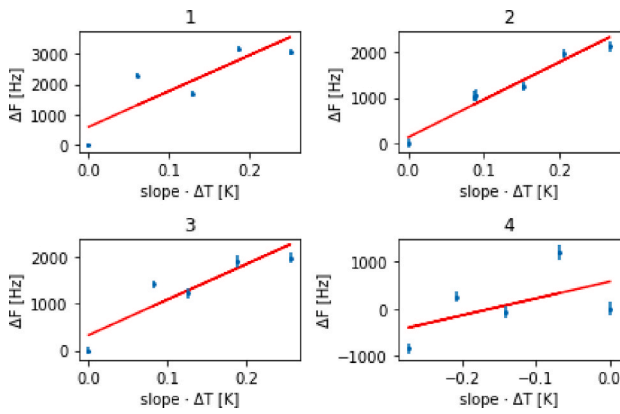


Fig. 6. 4 calibration curves obtained decreasing and increasing the temperature of the incubator without shielding from external field. For each step of temperature 10 data of \tilde{F} were acquired, then the standard deviation and the standard error were calculated and used to evaluate $\Delta \tilde{F}$. The resulting points are plotted and the linear fit, according to Equation (5), was evaluated.

Table 1

Coupling constant obtained without shielding from external fields.

| Data | $\gamma_T \left[\frac{\text{kHz}}{\text{K}} \right]$ | $\sigma \gamma_T \left[\frac{\text{kHz}}{\text{K}} \right]$ |
|------|---|--|
| 1 | 120 | 40 |
| 2 | 83 | 9 |
| 3 | 80 | 20 |
| 4 | 40 | 30 |

Table 2

Coupling constant obtained with the application of a Faraday cage.

| Data | $\gamma_T \left[\frac{\text{kHz}}{\text{K}} \right]$ | $\sigma \gamma_T \left[\frac{\text{kHz}}{\text{K}} \right]$ |
|------|---|--|
| 1 | 63 | 2 |
| 2 | 74 | 4 |
| 3 | 65 | 7 |
| 4 | 63 | 3 |

follow the same linear trend and consequently the uncertainty related to the coupling constant becomes smaller.

3.3. Discussion

The data we collected during the calibration of nanodiamonds for intracellular temperature measurements showed interesting differences depending on the shielding of the system from external electromagnetic noise. Without shielding, our measurements show a considerable scatter, and the uncertainty associated to γ_T was on average 36 %. On the other hand, when we used a Faraday cage to shield the system, our measurements exhibit a better compatibility with the linear regression. The uncertainty associated with the γ_T is reduced by an order of magnitude, showing that shielding effectively reduced the influence of external noise.

4. Conclusions

In conclusion, we have characterized the response of a set of nanodiamonds to temperature variations with the aim of determining γ_T , the coefficient linking temperature changes to resonance frequency variations. Our results indicate that the use of nanodiamonds as intracellular thermometers holds promise, but it is crucial to consider the influence of external electromagnetic noise on measurement accuracy. Employing a

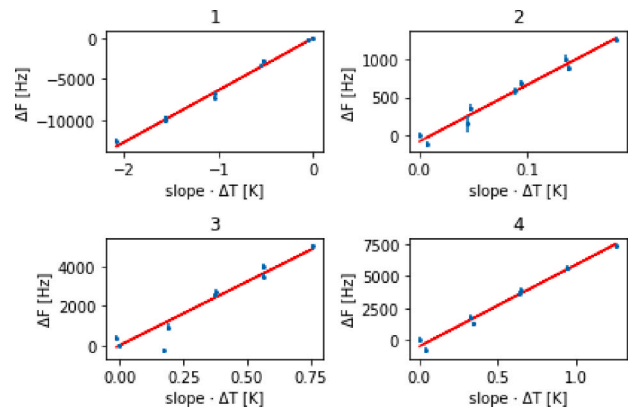


Fig. 7. 4 calibration curves obtained decreasing and increasing the temperature of the incubator enclosing the experimental setup in a Faraday cage.

Faraday cage has significantly reduced the uncertainty associated with the coupling coefficient γ_T , underlying the importance of shielding to enhance data reliability. Further research could focus on developing more effective shielding techniques and evaluating other factors that might impact intracellular measurements. However, overall, our findings support the use of nanodiamonds as intracellular thermometers with potential significant applications in biological and medical research.

Funding statement

This project (No. 20IND05) QADeT leading to this publication has received funding from the EMPIR program cofinanced by the Participating States and from the European Union's Horizon 2020 research and innovation program. The project was further supported OP RDE; Project CARAT (No.CZ.02.1.01/0.0/0.0/16.026/0008382), Compagnia di San Paolo, project TRAPEZIO QUAFUPHY, project INFN QUISS.

References

- [1] C. Abbattista, et al., Towards quantum 3D imaging devices, *Appl. Sci.* 11 (14) (Jul. 2021) 6414, <https://doi.org/10.3390/app11146414>.
- [2] G. Massaro, F. Di Lena, M. D'Angelo, F.V. Pepe, Effect of finite-sized optical components and pixels on light-field imaging through correlated light, *Sensors* 22 (7) (Apr. 2022) 2778, <https://doi.org/10.3390/s22072778>.
- [3] C. Abbattista, et al., Towards quantum 3D imaging devices, *Appl. Sci.* 11 (14) (Jul. 2021) 6414, <https://doi.org/10.3390/app11146414>.
- [4] L. Guarina, et al., Nanodiamonds-induced effects on neuronal firing of mouse hippocampal microcircuits, *Sci. Rep.* 8 (1) (Dec. 2018), <https://doi.org/10.1038/s41598-018-20528-5>.
- [5] G. Petrinì, et al., 'Is a Quantum Biosensing Revolution Approaching? Perspectives in NV-Assisted Current and Thermal Biosensing in Living Cells', *Advanced Quantum Technologies*, vol. 3, Wiley-VCH Verlag, Dec. 01, 2020, <https://doi.org/10.1002/quote.202000066>, 12.
- [6] R. Schirrhagl, K. Chang, M. Loretz, C.L. Degen, Nitrogen-vacancy centers in diamond: nanoscale sensors for physics and biology, *Annu. Rev. Phys. Chem.* 65 (1) (Apr. 2014) 83–105, <https://doi.org/10.1146/annurev-physchem-040513-103659>.
- [7] E. Nieto Hernández, et al., Efficiency optimization of Ge-V quantum emitters in single-crystal diamond upon ion implantation and HPHT annealing, *Adv. Quantum Technol.* 6 (8) (Aug. 2023), <https://doi.org/10.1002/quote.202300010>.
- [8] E. Corte, et al., Magnesium-vacancy optical centers in diamond, *ACS Photonics* 10 (1) (Jan. 2023) 101–110, <https://doi.org/10.1021/acsphotonics.2c01130>.
- [9] G. Kucsko, et al., Nanometre-scale thermometry in a living cell, *Nature* 500 (7460) (2013) 54–58, <https://doi.org/10.1038/nature12373>.
- [10] J.F. Barry, et al., Optical magnetic detection of single-neuron action potentials using quantum defects in diamond, *Proc. Natl. Acad. Sci. U. S. A.* 113 (49) (Dec. 2016) 14133–14138, <https://doi.org/10.1073/pnas.1601513113>.
- [11] M. Fujiwara, et al., Real-time nanodiamond thermometry probing in vivo thermogenic responses. <https://www.science.org>, 2020.
- [12] H.C. Davis, et al., Mapping the microscale origins of magnetic resonance image contrast with subcellular diamond magnetometry, *Nat. Commun.* 9 (1) (Dec. 2018), <https://doi.org/10.1038/s41467-017-02471-7>.
- [13] G. Petrinì, et al., Nanodiamond–quantum sensors reveal temperature variation associated to hippocampal neurons firing, *Adv. Sci.* 9 (28) (Oct. 2022), <https://doi.org/10.1002/advs.202202014>.

- [14] C. Robert, I. Hue, S. McGraw, D. Gagné, M.A. Sirard, Quantification of cyclin B1 and p34cdc2 in bovine cumulus-oocyte complexes and expression mapping of genes involved in the cell cycle by complementary DNA macroarrays, *Biol. Reprod.* 67 (5) (Nov. 2002) 1456–1464, <https://doi.org/10.1095/biolreprod.102.002147>.
- [15] L. De Meis, L.A. Ketzer, R.M. Da Costa, I.R. De Andrade, M. Benchimol, Fusion of the endoplasmic reticulum and mitochondrial outer membrane in rats brown adipose tissue: activation of thermogenesis by Ca²⁺, *PLoS One* 5 (3) (Mar. 2010) <https://doi.org/10.1371/journal.pone.0009439>.
- [16] T. Sekiguchi, S. Sotoma, Y. Harada, Fluorescent nanodiamonds as a robust temperature sensor inside a single cell, *Biophys. Physicobiol.* 15 (0) (2018) 229–234, https://doi.org/10.2142/biophysico.15.0_229.
- [17] A. Lenef, S.C. Rand, Electronic structure of the N- V center in diamond: theory, *Phys. Rev. B* 53 (20) (May 1996) 13441–13455, <https://doi.org/10.1103/PhysRevB.53.13441>.
- [18] M.W. Doherty, et al., Theory of the ground-state spin of the NV center in diamond, *Phys. Rev. B* 85 (20) (May 2012) 205203, <https://doi.org/10.1103/PhysRevB.85.205203>.
- [19] T.F. Segawa, R. Igarashi, Nanoscale quantum sensing with Nitrogen-Vacancy centers in nanodiamonds – a magnetic resonance perspective, *Prog. Nucl. Magn. Reson. Spectrosc.* 134 (135) (Apr. 2023) 20–38, <https://doi.org/10.1016/j.pnmrs.2022.12.001>.
- [20] Z. Zhang, R. Xu, Y. Zhang, B. Du, K. Huang, L. Cheng, Design of NV centers integrated magnetometer and high-resolution output module based on the ODMR system, *IEEE Sensor. J.* 23 (6) (Mar. 2023) 6150–6155, <https://doi.org/10.1109/JSEN.2023.3240885>.
- [21] M.W. Doherty, et al., Electronic properties and Metrology applications of the diamond NV center under pressure, *Phys. Rev. Lett.* 112 (4) (Jan. 2014) 047601, <https://doi.org/10.1103/PhysRevLett.112.047601>.
- [22] S. Hong, et al., Nanoscale magnetometry with NV centers in diamond, *MRS Bull.* 38 (2) (Feb. 2013) 155–161, <https://doi.org/10.1557/mrs.2013.23>.
- [23] E. Moreva, et al., Practical applications of quantum sensing: a simple method to enhance the sensitivity of nitrogen-vacancy-based temperature sensors, *Phys. Rev. Appl.* 13 (5) (May 2020) 054057, <https://doi.org/10.1103/PhysRevApplied.13.054057>.
- [24] M.W. Doherty, et al., Temperature shifts of the resonances of the NV center in diamond, *Phys. Rev. B* 90 (4) (Jul. 2014) 041201, <https://doi.org/10.1103/PhysRevB.90.041201>.
- [25] V.M. Acosta, E. Bauch, M.P. Ledbetter, A. Waxman, L.S. Bouchard, D. Budker, Temperature dependence of the nitrogen-vacancy magnetic resonance in diamond, *Phys. Rev. Lett.* 104 (7) (Feb. 2010), <https://doi.org/10.1103/PhysRevLett.104.070801>.
- [26] X.-D. Chen, et al., Temperature dependent energy level shifts of nitrogen-vacancy centers in diamond, *Appl. Phys. Lett.* 99 (16) (Oct. 2011), <https://doi.org/10.1063/1.3652910>.
- [27] S. Sotoma, et al., In situ measurements of intracellular thermal conductivity using heater-thermometer hybrid diamond nanosensors, *Sci. Adv.* 7 (3) (Jan. 2021), <https://doi.org/10.1126/sciadv.abd7888>.
- [28] D.A. Simpson, et al., Non-neurotoxic nanodiamond probes for intraneuronal temperature mapping, *ACS Nano* 11 (12) (Dec. 2017) 12077–12086, <https://doi.org/10.1021/acsnano.7b04850>.
- [29] H. Yukawa, et al., A quantum thermometric sensing and analysis system using fluorescent nanodiamonds for the evaluation of living stem cell functions according to intracellular temperature, *Nanoscale Adv.* 2 (5) (2020) 1859–1868, <https://doi.org/10.1039/D0NA00146E>.
- [30] L. Guarina, et al., Nanodiamonds-induced effects on neuronal firing of mouse hippocampal microcircuits, *Sci. Rep.* 8 (1) (Dec. 2018), <https://doi.org/10.1038/s41598-018-20528-5>.
- [31] A. Alessio, E. Bernardi, E. Moreva, I. Pietro Degiovanni, M. Genovese, M. Truccato, Limitations of bulk diamond sensors for single-cell thermometry, *Sensors* 24 (1) (Dec. 2023) 200, <https://doi.org/10.3390/s24010200>.
- [32] S.K.R. Singam, M. Nesladek, E. Goovaerts, Nitrogen-vacancy nanodiamond based local thermometry using frequency-jump modulation, *Nanotechnology* 31 (10) (Mar. 2020) 105501, <https://doi.org/10.1088/1361-6528/ab5a0c>.
- [33] K. Sasaki, et al., Broadband, large-area microwave antenna for optically detected magnetic resonance of nitrogen-vacancy centers in diamond, *Rev. Sci. Instrum.* 87 (5) (May 2016), <https://doi.org/10.1063/1.4952418>.

Claudia Stella^{a,b,*}, Ekaterina Moreva^b, Ettore Bernardi^b, Elena Losero^b,
Paolo Traina^b, Ivo Pietro Degiovanni^b, Giulia Tomagra^{c,d},
Valentina Carabelli^{c,d}, Petr Cígler^e, Marco Genovese^b
^a Politecnico di Torino, 10129, Turin, Italy
^b Istituto Nazionale di Ricerca Metrologica, 10135, Turin, Italy
^c Department of Drug and Science Technology, University of Torino, 10125,
Turin, Italy
^d NIS Inter-departmental Centre, 10135, Turin, Italy
^e Institute of Medical Biochemistry and Laboratory Diagnostics, 166 10,
Prague, Czech Republic

* Corresponding author. Politecnico di Torino, 10129, Turin, Italy.
E-mail address: claudia.stella@polito.it (C. Stella).